ACS APPLIED MATERIALS & INTERFACES

Research Article

www.acsami.org

Co Nanoparticles Induced Resistive Switching and Magnetism for the Electrochemically Deposited Polypyrrole Composite Films

Zedong Xu,[†] Min Gao,[†] Lina Yu,[†] Liying Lu,[‡] Xiaoguang Xu,*[,†] and Yong Jiang*[,†]

[†]State Key Laboratory for Advanced Metals and Materials, School of Materials Science and Engineering, and [‡]School of Chemical and Biological Engineering, University of Science and Technology Beijing, Beijing 100083, People's Republic of China

Supporting Information

ABSTRACT: The resistive switching behavior of Co-nanoparticle-dispersed polypyrrole (PPy) composite films is studied. A novel design method for resistive random access memory (ReRAM) is proposed. The conducting polymer films with metal nanocrystal (NC)-dispersed carbon chains induce the spontaneous oxidization of the conducting polymer at the surface. The resistive switching behavior is achieved by an electric field controlling the oxygen ion mobility between the metal electrode and the conducting polymer film to realize the mutual transition between intrinsic conduction (low resistive state) and oxidized layer conduction (high resistive state). Furthermore, the formation process of intrinsic conductive paths can be effectively controlled in the conducting polymer ReRAM using metal NCs in films because the inner metal NCs induce electric field lines converging around them and the intensity of the electric field at the tip of NCs can greatly exceed that of the other region. Metal NCs can also bring new characteristics for ReRAM, such as magnetism by dispersing magnetic metal NCs in polymer, to obtain multifunctional electronic devices or meet some special purpose in future applications. Our works will enrich the application fields of the electromagnetic PPy composite films and present a novel material for ReRAM devices.

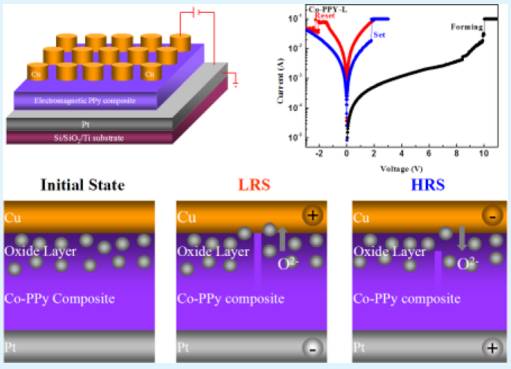

KEYWORDS: *conducting polymer, polypyrrole composite films, XPS depth profiling, magnetism, resistive switching, oxygen ion migration*

1. INTRODUCTION

The demands for higher integration density and advanced device performance are continuously increasing because of the theoretical and physical limit of conventional Si-based technologies. The novel nonvolatile memory devices are principally based on the bi- or multistability of devices, such as magnetic random access memory (MRAM),[1] ferroelectric random access memory (FeRAM),[2] resistive random access memory (ReRAM),[3] etc. They combine the advantages of flash memory and dynamic random access memory (DRAM) while avoiding their drawbacks, so that they might be highly scalable. Organic and polymer-based resistive memory cells sandwiched between two vertically aligned electrodes constitute crossbar memory arrays, in which the building blocks, referred to as bit cells, possess two or multiple stable resistance states.[4−7] They are promising circuit elements because of their good scalability and processability, high possibility of molecular design through chemical synthesis, high storage density, amenability to processing onto a variety of substrates, and large-area and low-cost deposition techniques, such as spin coating, roll-to-roll processing, ink jet printing, and electrochemical processing.[8] Additionally, the polymer also presents other favorable properties working as special electronic devices, such as excellent mechanical strength, lightweight, and flexibility.[4,9]

The polypyrrole (PPy) is a kind of conducting polymer with high conductivity, relatively good environmental stability, and easy preparation under various conditions. The electromagnetic PPy composite films in comparison to pure PPy have more degrees of freedom, electrical and magnetic, which makes them present more rich characteristics.[10,11] Therefore, they have attracted great attention because of their various potential applications, such as microwave absorbing materials, adsorption materials, electrocatalytic reagents to biospecies, and specialized contrast agents for ^{1}H magnetic resonance imaging, magnetic separation of genomic DNA, cancer cell targeting, biosensors, etc.[10]

In this paper, the resistive switching feature of the electromagnetic PPy composite films with magnetic metal cobalt nanoparticles (Co NPs) is investigated for the first time. The Co−PPy composite films are prepared by electrochemical depositing, which is a cost-effective, versatile, and highly controllable method, ideally adapted to the engineering of nanostructured materials. The pure PPy film does not show any resistive switching phenomenon, while the Co−PPy composite films show obvious bipolar resistive switching with a typical

Received: July 9, 2014
Accepted: September 23, 2014
Published: September 23, 2014

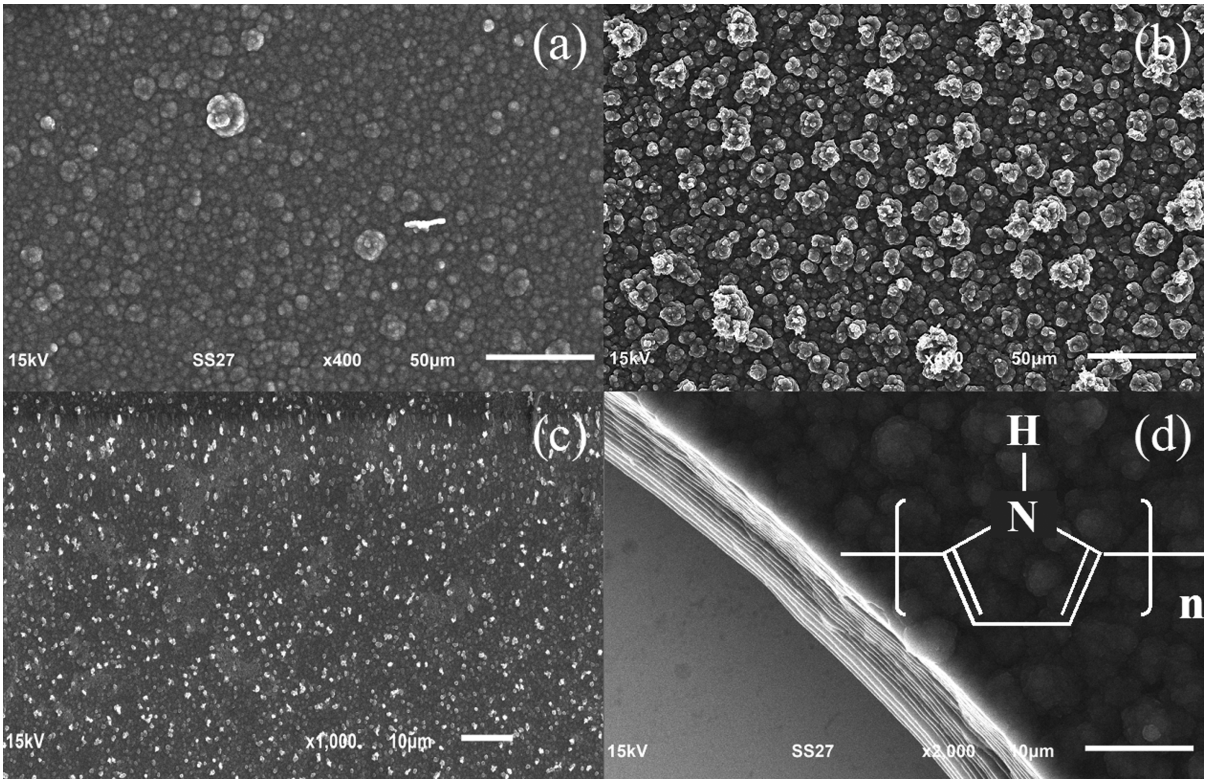

Figure 1. SEM micrographs of the samples: (a) pure PPy, (b) Co−PPy-L, and (c) Co−PPy-H. (d) Cross-sectional SEM image of the pure PPy sample. The inset of panel d is the molecular structure of PPy.

filamentary feature. The role of the Co NPs for resistive switching in the Co−PPy composite films and the detailed mechanism are discussed.

2. EXPERIMENTAL SECTION

2.1. Preparation of Co NPs. The preparation of Co NPs has been depicted in our previous work.[12]

2.2. Synthesis of PPy Films. The PPy films with different contents of Co NPs were electrochemically polymerized onto Si/SiO_2/Ti/Pt substrates from acidic aqueous solutions. The Si/SiO_2/Ti/Pt substrates had been ultrasonically cleaned in acetone and isopropanol in turn. The electrolyte was composed of 0.1 mol/L anhydrous sodium sulfate, 0.001 mol/L sodium dodecylbenzenseulfonate, and 0.1 mol/L pyrrole. The pH value was adjusted to 3 by adding sulfuric acid. All electropolymerizations were performed at room temperature in a conventional three-electrode cell with a platinum counter electrode and a saturated calomel electrode (SCE) coupled to a fine Luggin capillary as a reference electrode. Before electropolymerization, several drops of well-dispersed Co NP suspension were added to the electrolyte and stirred sufficiently. The adding amounts for pure PPy film (expressed as PPy sample), low-content Co NP PPy film (expressed as Co−PPy-L sample), and high-content Co NP PPy film (expressed as Co−PPy-H sample) were 0, 5, and 50 drops, respectively. The electropolymerizations were carried out by cyclic voltammetry. The potential was swept between 0.5 and 1.0 V at a 250 mV/s rate for 30 successive cycles. The as-deposited films were then washed by deionized water repeatedly and dried in the air.

2.3. Preparation of Electrodes. The 200 nm thick Cu top electrodes were deposited on the films by direct current (DC) magnetron sputtering at room temperature with a shadow mask (diameter = 200 μm). Voltages were applied to the Cu top electrode (TE), with the Pt bottom electrode (BE) grounded the entire time.

2.4. Sample Characterization. The crystal structures were analyzed by X-ray diffraction (XRD, Panalytical PW3040/60) equipped with Cu Kα radiation (λ = 1.504 05 Å). The morphology and dimensions of the films were examined with a JEOL 6510 scanning electron microscope (SEM). The chemical valence of elements was investigated by Kratos AXIS ULTRA DLD X-ray photoelectron spectroscopy (XPS). The magnetic hysteresis loops were measured by a quantum design physical property measurement system (PPMS) at room temperature. Electric measurements were carried out on a Keithley 4200-SCS semiconductor parameter analyzer.

3. RESULTS AND DISCUSSION

3.1. Structures and Morphologies of Films. The high-quality electromagnetic PPy composite film is the key for the practical electronic device applications. Although there are many preparation methods for electromagnetic PPy composite films, the optimal film deposition way is the electrochemical synthesis in the presence of magnetic additives.[13] The cyclic voltammetry can obtain smoother and more compact films than electrochemically depositing under constant potentials. Therefore, we choose cyclic voltammetry to prepare PPy films in our experiment. Panels a−c of Figure 1 give the surface morphologies of the pure PPy, Co−PPy-L, and Co−PPy-H films, respectively. All of the films are continuous and compact, especially for the Co−PPy-H film. It is because the growing polymer chains are supported by the magnetic crystals, leading to an improved compactness.[14] The cross-sectional SEM image in Figure 1d reveals the lamellar structure and layer-by-layer depositing process for the pure PPy film. The cross-sectional images of the Co−PPy-L and Co−PPy-H films, which are not shown here, are similar to that of the pure PPy film. The layer number is consistent with the cycle number of cyclic voltammetry, which proves that the thickness of films could be tailored by designing the cycle number in the electrochemical depositing process. The structures are determined by the XRD patterns of the films (see Figure S1 of the Supporting

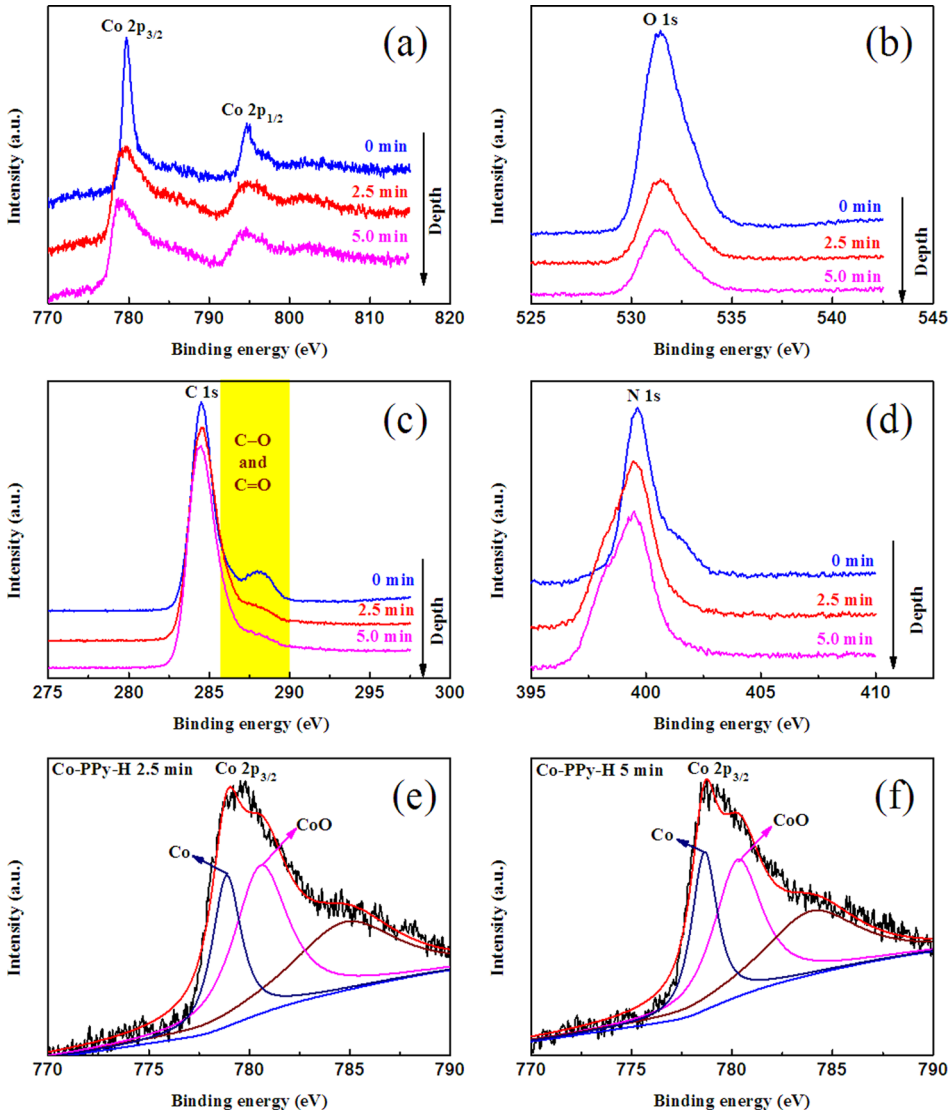

Figure 2. XPS depth profiling analysis of the Co–PPy-H sample after various Ar sputtering etching times: (a) Co 2p, (b) O 1s, (c) C 1s, (d) N 1s, and (e and f) Co $2p_{3/2}$ XPS spectra and fitting results of the 2.5 and 5 min curves, respectively.

Information). Only a broad halo peak and the sharp order peaks of the $Si/SiO_2/Ti/Pt$ substrates are observed without any peak related to the crystalline phase of the PPy or Co NPs, indicating that the as-deposited pure PPy, Co NPs, and Co–PPy composite films are all amorphous.

To further analyze the distribution of Co NPs in the Co–PPy composite films, more direct evidence of the distribution is obtained from analyzing the chemical states with dependence upon the depth. The Co–PPy-H sample is chosen to probe the chemical states of each chemical element, because the more content of Co brings a higher peak intensity of XPS that gives more accurate measurement results. Panels a–d of Figure 2 show the depth profiling analysis of the as-deposited Co–PPy-H sample, obtained by collecting Co 2p, O 1s, C 1s, and N 1s XPS spectra from different depths after Ar ion beam etching at different times, respectively. The Ar etching rate is kept to be 3 nm/min. In Figure 2a, the Co $2p_{3/2}$ peak at 780.4 eV and Co $2p_{1/2}$ peak at 795.6 eV of CoO have relatively strong intensities at the surface. No Co $2p_{3/2}$ peak at 778.3 eV and Co $2p_{1/2}$ peak at 793 eV of Co metal can be observed at the surface, indicating that the surface Co atoms are almost completely oxidized. Inside the film, three chemical states of Co could be found after deconvolution of the Co $2p_{3/2}$ peaks: metallic Co, CoO, and an unknown peak located at 778.3, 780.4, and above 784.3 eV, respectively (panels e and f of Figure 2). The unknown peak may originate from the formation of the coordination bond between Co^{2+} and –NH of PPy chains.[15] The peak intensities of Co 2p show little variations with the depth increase, except the one at the surface. It demonstrates that the Co NPs are uniformly dispersed within PPy films. The Co NPs are oxidized into the CoO/Co structure because of the deposition process carried out in aqueous solution. Co has a tendency to form a coordination bond with –NH of PPy chains, and the PPy films prevent the further oxidization of Co NPs in external environmental conditions. In both the surface and interior of the film, the O 1s peak could be detected for the Co–PPy-H sample, as shown in Figure 2b. The surface peak intensity is much stronger than the internal peak intensity, and the internal peak intensity is an approximate constant with the depth increase. We conclude that the PPy is also partially oxidized at the surface, not only Co NPs. For the C 1s spectrum in Figure 2c, the obvious double peaks are observed at the surface but

dx.doi.org/10.1021/am5044399 | ACS Appl. Mater. Interfaces 2014, 6, 17823–17830

only one peak is present within the film. The fitting result of the C 1s XPS peak gives three peak positions of about 284.6, 285.7, and 288.0 eV, corresponding to C−H/C−N, hydroxy (C−O), and carbonyl (C═O), respectively (see Figure S3 of the Supporting Information).[16] It means that there is a difference between the chemical states of the surface and the interior, which is consistent with the oxidization of the PPy at surface. The XPS peaks of hydroxy and carbonyl are not obvious within the film, indicating little oxidization within the film; therefore, the surface oxidization comes from the external environment. The N 1s spectrum given in Figure 2d shows an obvious change from the surface to the interior. From the interior to the surface, the N 1s peak shifts to higher energy, because of the charge transfer interactions with oxygen,[17] which further verifies oxidization of PPy at the surface and less oxidization within the film. By comparing the XPS peak intensity of each chemical element, we estimate that the Co atomic content is about 1.55% within the Co−PPy-H sample and that of the surface is lower than that of the interior. The Co atomic content is inferred about 0.155% within the Co−PPy-L sample based on the same deposition process and suspension of well-dispersed Co NPs in every drop with the Co−PPy-H film.

3.2. Magnetic Properties. The magnetic properties of the PPy composite films are mainly determined by the magnetic crystal additives.[10] Figure 3 gives the magnetic hysteresis loops

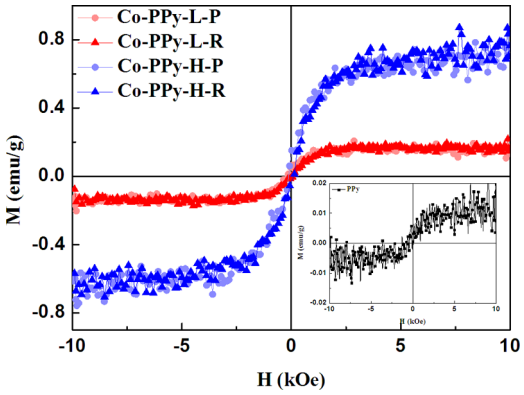

Figure 3. Magnetic hysteresis loops of the pure PPy, Co−PPy-L, and Co−PPy-H samples measured at room temperature.

of the pure PPy, Co−PPy-L, and Co−PPy-H samples, respectively. The M−H curves show that the pure PPy is nonmagnetic and the Co−PPy films possess magnetism. The approximate zero coercivity and reversible hysteresis behavior are observed, indicating the superparamagnetic nature of the Co−PPy composite films similar to that of pure Co NPs because of their mean diameter of less than 10 nm (see Figure S2 of the Supporting Information). It demonstrates that the Co NPs do not aggregate after the depositing process of the Co−PPy composite films. The saturation magnetization M_s of the Co−PPy composite films greatly depends upon the content of the Co NPs. For PPy composite, the saturation magnetization M_s can be expressed by the empirical formula $M_s = Vm_s$, where V is the volume fraction of magnetic NPs and m_s is the saturation magnetization of magnetic NPs.[18] As the volume fraction of magnetic NPs increases, the saturation magnetization of the composite films increases, as known from the formula. However, in our case, M_s is not accurately proportional to the volume fraction of Co NPs, which is due to the demagnetization effect of PPy and the oxidization of Co NPs.

3.3. Switching Property. Figure 4a shows a schematic diagram of the sample layout and the measurement configuration. For all devices, the positive bias voltage is applied to the top Cu electrodes and a current compliance is set at 0.1 A to prevent the devices. Panels b−d of Figure 4 depict typical $I-V$ curves for the pure PPy, Co−PPy-L, and Co−PPy-H samples on a semi-logarithmic scale, respectively. The pure PPy sample is a good conductor, and no switching behavior is observed, as shown in Figure 4b. In Figure 4c, for the Co−PPy-L sample, an abrupt increase of the current can be observed, while a 10 V positive bias voltage is applied, namely, the forming process or the first set process, for which the resistance of the device is changed from the initial resistance state to a low resistance state (LRS), owing to the formation of conducting filaments. After the electroforming process, an applied −1.9 V negative bias voltage drives the resistance back to a high resistance state (HRS), called the reset process, implying the rupture of conducting filaments. Then, a typical bipolar resistive switching curve is achieved by sweeping the bias voltage as 0 → +3 → 0 → −3 → 0 V, with a set process and a reset process. From the second sweep cycle, both the set voltage and the absolute value of the reset voltage are less than 2.5 V. The Co−PPy-H sample presents similar switching phenomenon in the same operating process as the Co−PPy-L sample, as shown in Figure 4d. However, the set and reset voltages of the Co−PPy-H sample are less than those of the Co−PPy-L sample, and the switching is not stable. We have tried many different cells for Co−PPy-H films, and every cell only realizes 5−10 switching cycles. The possible reason is discussed in section 3.4.

Successive 100 switching cycles have been performed in a Co−PPy-L device, and the statistical analysis is made to obtain further information on the switching stability, as shown in panels a and b of Figure 5. The Co−PPy-L memory device exhibits excellent stability in its resistive switching behavior and a very narrow distribution of both set voltage (V_{set}, from 1.07 to 2.3 V) and reset voltage (V_{reset}, from −1.29 to −2.3 V). In comparison to other traditional ReRAM,[19,20] the Co−PPy-L memory device shows a narrower distribution of V_{set} and V_{reset} for a single memory cell, which is very important for accurately controlling the writing and erasing of information. The resistances of both HRS and LRS scatter to a certain extent during cycling and exhibit a broad range of dispersions at V_{read} = 0.2 V. Although the mean on/off current ratio is low, the large current density supplies a sufficient read current in a nanoscale memory cell to allow for a fast detection of the state by reasonably small sense amplifiers.[21] The stable retention performance of the structure has also been confirmed at room temperature for 10^4 s for both HRS and LRS, as shown in Figure 5c. Judging from the present trend of data, the information storage in this structure is likely to persist for an even longer time, revealing the reliability of the bipolar resistive switching effect.

3.4. Detailed Mechanism of Switching. To further understand the conduction and switching behaviors of the Co−PPy-L sample, some possible mechanisms, for example, Ohmic conduction, space-charge-limited conduction (SCLC), interface-limited Schottky emission, bulk-limited Poole−Frenkel (PF) emission, and interface-limited Fowler−Nordheim (F−N) tunneling, have been used to fit its $I-V$ curves. Figure 6a shows the fitting results of the LRS and HRS in the positive bias voltage region for the Co−PPy-L sample. The fitting results for the LRS and HRS demonstrate that the charge transport behavior is in good agreement with a classical trap-

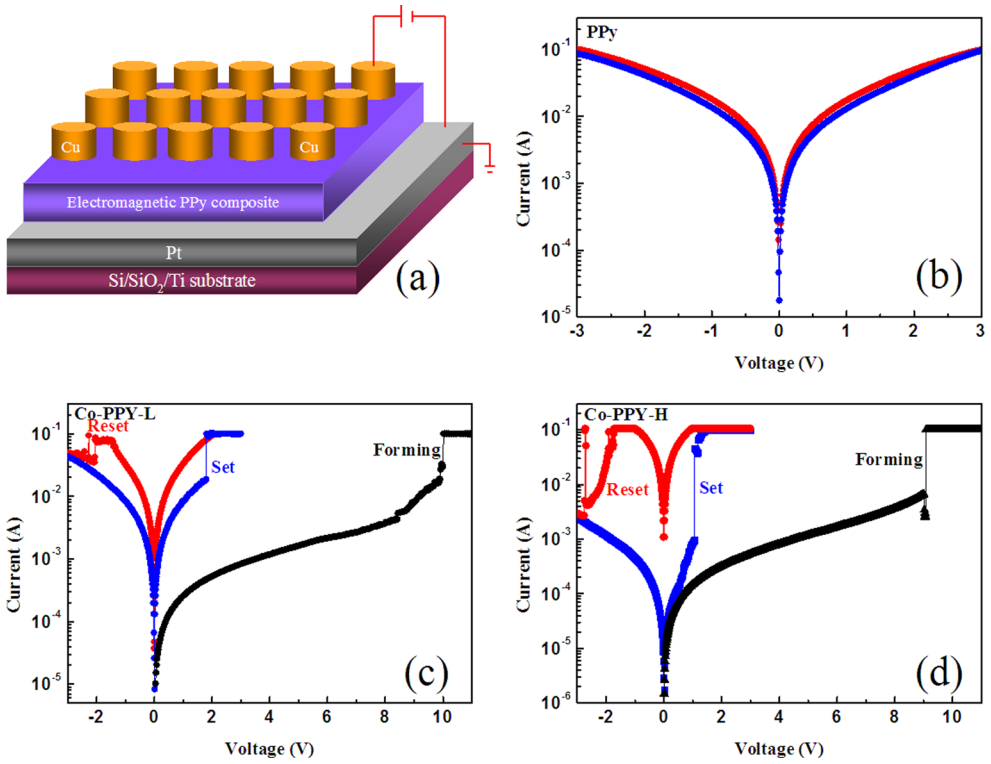

Figure 4. (a) Schematic diagram of the sample layout and measurement configuration. (b) No switching $I-V$ curve of the pure PPy sample. (c and d) Typical $I-V$ curves of the bipolar resistive switching behavior with forming process for the Co−PPy-L and Co−PPy-H samples, respectively.

controlled SCLC described by a simple equation of $I(V) = aV + bV^2$.[22] The conduction behavior of the LRS is not Ohmic conduction, and the resistances of the LRS exhibit a broad range of dispersions compared to atomic switching,[19,20] proving no electrochemical metallization of Cu electrodes to form metallic filaments. The $I-V$ curve of the pure PPy sample is fitted, and the result is also in good agreement with SCLC, as shown in Figure 6b.

When the current values of the pure PPy, Co−PPy-L, and Co−PPy-H samples for HRS and LRS at V_{read} = 0.2 V are compared to the increasing content of Co NPs, the current increases for LRS and decreases for HRS, as shown in Figure 7. The tendency of conductivity in LRS agrees with some reported results at the low content region of the magnetic crystal.[23−25] The conductivity increases with the increased doping level of PPy, compactness of the samples, and PPy content. The doping level is calculated from the ratio of the peak area of N^+ to the total of N 1s in PPy and Co−PPy composite films.[22] Generally, N atoms of PPy chains are divided into three different nitrogen species, namely, the imine-like (=NH−), amine-like (−NH−), and positively charged nitrogen (N^+) structures, and the XPS peaks are located in 398.6, 399.8, and above 400 eV, respectively.[16,26] The deconvoluted results of the N 1s core-level spectrum and the obtained doping level are shown in panels a−c of Figure 8. The doping levels are 0.272, 0.280, and 0.332, corresponding to the pure PPy, Co−PPy-L, and Co−PPy-H samples, respectively, which agree with the tendency of conductivity in LRS. Furthermore, the conductive behaviors of the Co−PPy in LRS are similar to the conductive behavior of pure PPy samples; in that, all $I-V$ curves are in good agreement with SCLC. This proves that the conductance derives from the intrinsic part of PPy in LRS for the three samples rather than the charge trapping/detrapping with Co NPs.[27] However, the conductivity of HRS decreases as the content of Co NPs increases, showing an opposite trend with the doping level. Figure S3 of the Supporting Information give the C 1s XPS spectra at surfaces of the pure PPy, Co−PPy-L, and Co−PPy-H samples. As the content of Co NPs increases, the XPS peak intensities of hydroxy and carbonyl carbon become increasingly strong, which implies that Co NPs may induce the oxidization of PPy at the surface. It leads to the production of some hydroxy and carbonyl groups and disrupts the conjugation, even causing ring opening, which causes the conductivity decrease, and the initial resistance at the surface is determined by the oxide layer. In comparison of the XPS peak intensities of O 1s and N 1s at the surface, the atomic ratios are 1:1, 1.6:1, and 2.63:1 for the pure PPy, Co−PPy-L, and Co−PPy-H samples, respectively, which further certifies easier oxidization for the PPy being inserted by a higher content of Co NPs at the surface. This may be because PPy and metal Co form local primary batteries or Co NPs work as a catalyst of the oxidation reaction, inducing the oxidization of PPy at the surface. Nonetheless, the reasons are unclear and will be further explored in our future study.

The detailed mechanism of the resistive switching behavior is proposed in panels a−c of Figure 9. The resistance of the initial state is determined by the one of the oxide layers for the pure PPy, Co−PPy-L, and Co−PPy-H samples. Applying a positive bias voltage to the top electrode, the oxygen ions at the surface migrate toward the Cu electrode to form local intrinsic PPy conductive filaments under the electric force, resulting in the jump from the HRS to LRS. Therefore, this process requires a forming process with a large bias voltage similar to oxygen ion migration switching.[28−30] Subsequently, a sufficient opposite polarity bias voltage applied can rupture the filaments to

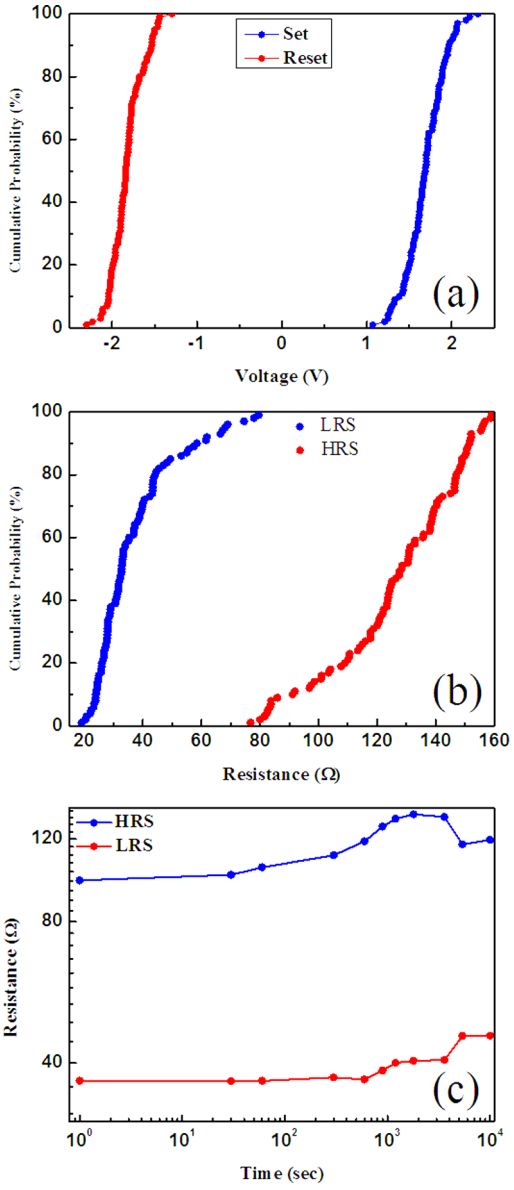

Figure 5. Cumulative probability of (a) threshold voltage and (b) resistance for both HRS and LRS under a read bias of 0.2 V. (c) Retention property of both HRS and LRS under a read bias of 0.2 V.

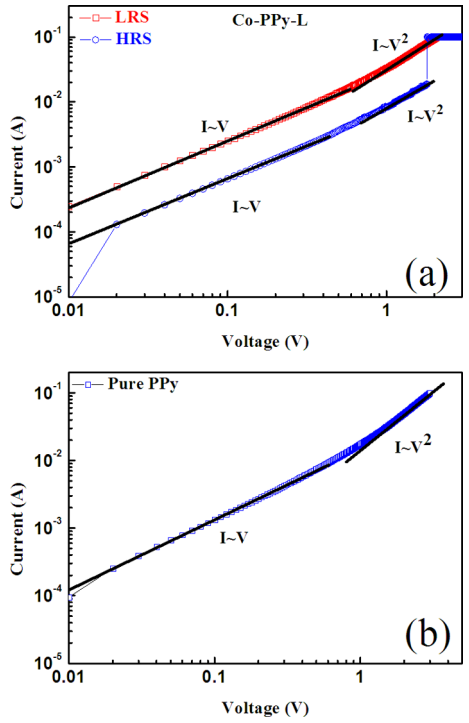

Figure 6. (a) Fitting results of the HRS and LRS for the *I*−*V* curves in the positive voltage region of the Co−PPy-L sample. (b) Fitting result for the *I*−*V* curves in the positive voltage region of the pure PPy sample.

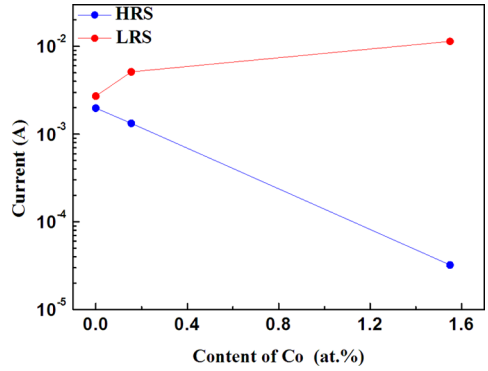

Figure 7. Current of both HRS and LRS as a function of the Co atomic content.

sharply switch the device resistance back to the HRS, because the oxygen ions come back to PPy and reconstruct the oxide layer with it. The resistive switching behavior is achieved by the electric field force controlling the oxygen ion mobility between the Cu electrode and the Co−PPy composite film to realize the mutual transition between intrinsic conduction (LRS) and oxidized layer conduction (HRS). For the pure PPy sample, there is little difference of resistance between the oxide layer and PPy because of less oxidization, so that no obvious switching is observed. For the Co−PPy-L and Co−PPy-H samples, overoxidization makes a huge distinction of resistance between the oxide layer and PPy to realize resistive switching. The conductive or semi-conductive CoO/Co NPs dispersed in PPy films induce electric field lines converging around the NP sites, and the intensity of the electric field at the tip of NPs can greatly exceed that of the other region.[31,32] Because of the NP-enhanced electric field, the oxygen ions around the NP locations are easier to migrate toward the top electrode and form local filaments along the shortest path consisting of Co NPs than other regions, which enables their formation probability along the same path during repeating resistive switching cycles to make a narrower distribution of V_{set} and V_{reset}.[31] For the Co−PPy-H sample, the switching is not stable, which may be due to the large resistance of HRS generating more heat to invalidate polymer chains.

4. CONCLUSION

We successfully prepared the electromagnetic PPy composite films with different contents of Co NPs by electrochemical depositing. The Co−PPy composite films present obvious magnetism compared to the pure PPy sample. The stable bipolar resistance switching is observed in the Co−PPy composite film with a low content of Co NPs. Analyzing the results of XPS, we found that the resistance switching behavior is due to the electric field force controlling the oxygen ion

dx.doi.org/10.1021/am5044399 | ACS Appl. Mater. Interfaces 2014, 6, 17823−17830

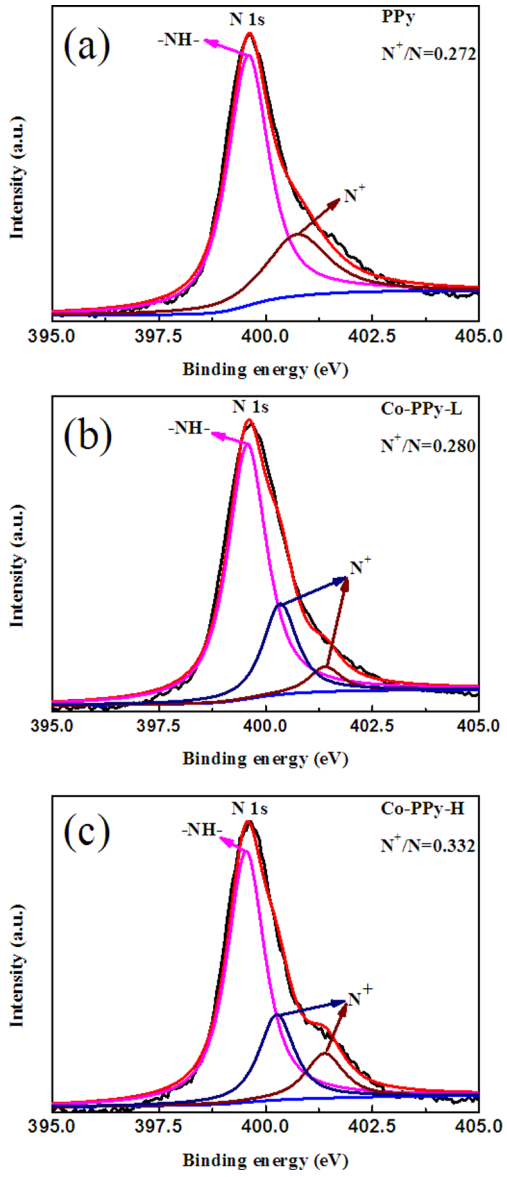

Figure 8. N 1s XPS spectra and fitting results of (a) pure PPy, (b) Co−PPy-L, and (c) Co−PPy-H samples at the surface.

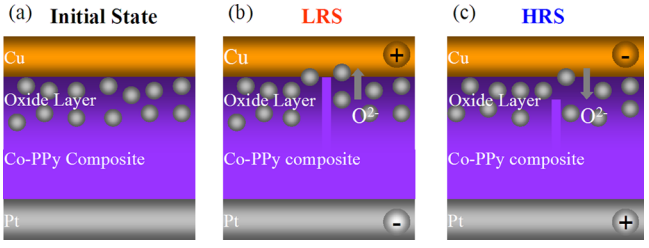

Figure 9. Schematic pictures of the resistive switching: (a) initial state, (b) LRS and set process, and (c) HRS and reset process.

mobility between the Cu electrode and PPy films to realize the mutual transition between intrinsic conduction and oxidized layer conduction. The conductivity is rooted in the intrinsic conduction of PPy in LRS and oxide layer conduction of PPy in HRS. The PPy oxide layer at the surface is induced by metal Co NPs. The filament formation process is effectively controlled in the Co−PPy composite ReRAM devices using Co NPs dispersed in PPy films. We conclude that filaments grow easily along the shortest path consisting of NPs, which enables their formation probability along the same path during repeating resistive switching cycles and makes the memory devices more controllable. The electromagnetic Co−PPy composite devices simultaneously present magnetism and resistive switching peculiarity and permit the buildup of new multifunctional electronic devices or some special purpose in future applications.

■ ASSOCIATED CONTENT

Ⓢ Supporting Information

XRD patterns of the pure PPy, Co−PPy-L, and Co−PPy-H samples (Figure S1), TEM image and magnetic hysteresis loops of Co NPs (Figure S2), and C 1s XPS spectrum and fitting result of the Co−PPy-H sample at the surface position and C 1s XPS spectra of the pure PPy, Co−PPy-L, and Co−PPy-H samples at the surfaces (Figure S3). This material is available free of charge via the Internet at http://pubs.acs.org.

■ AUTHOR INFORMATION

Corresponding Authors

*E-mail: xgxu@ustb.edu.cn.
*E-mail: yjiang@ustb.edu.cn.

Notes

The authors declare no competing financial interest.

■ ACKNOWLEDGMENTS

This work was partially supported by the National Basic Research Program of China (Grants 2012CB932702 and 2015CB921502), the National Science Foundation of China (Grants 11174031, 51371024, 51325101, 51271020, 51471029, and 61471036), PCSIRT, Beijing Nova Program (Grant 2011031), and the Fundamental Research Funds for the Central Universities (FRF-TP-12-010B).

■ REFERENCES

(1) Inomata, K. Present and future of magnetic RAM technology. *IEICE Trans. Fundam. Electron., Commun. Comput. Sci.* **2001**, *E84-C*, 740−746.
(2) Scott, J. F.; Araujo, C. A. Ferroelectric memories. *Science* **1989**, *246*, 1400−1405.
(3) Waser, R.; Aono, M. Nanoionics-based resistive switching memories. *Nat. Mater.* **2007**, *6*, 833−840.
(4) Cho, B.; Yun, J. M.; Song, S.; Ji, Y.; Kim, D. Y.; Lee, T. Organic resistive memory devices: Performance enhancement, integration, and advanced architectures. *Adv. Funct. Mater.* **2011**, *21*, 3976−3981.
(5) Stewart, D. R.; Ohlberg, D. A. A.; Beck, P. A.; Chen, Y.; Williams, R. S.; Jeppesen, J. O.; Nielsen, K. A.; Stoddart, J. F. Molecule-independent electrical switching in Pt/organic monolayer/Ti devices. *Nano Lett.* **2004**, *4*, 133−136.
(6) Wu, S. M.; Tsuruoka, T.; Terabe, K.; Hasegawa, T.; Hill, J. P.; Ariga, K.; Aono, M. A polymer-electrolyte-based atomic switch. *Adv. Funct. Mater.* **2011**, *21*, 93−99.
(7) Liu, S. J.; Wang, P.; Zhao, Q.; Yang, H. Y.; Wong, J.; Sun, H. B.; Dong, X. C.; Lin, W. P.; Huang, W. Single polymer-based ternary electronic memory material and device. *Adv. Mater.* **2012**, *24*, 2901−2905.
(8) Altebaeumer, T.; Gotsmann, B.; Pozidis, H.; Knoll, A.; Duerig, U. Nanoscale shape-memory function in highly cross-linked polymers. *Nano Lett.* **2008**, *8*, 4398−4403.
(9) Lai, Y. C.; Wang, Y. X.; Huang, Y. C.; Lin, T. Y.; Hsieh, Y. P.; Yang, Y. J.; Chen, Y. F. Rewritable, moldable, and flexible sticker-type organic memory on arbitrary substrates. *Adv. Funct. Mater.* **2014**, *24*, 1430−1438.

(10) Xiao, H. M.; Fu, S. Y. Synthesis and physical properties of electromagnetic polypyrrole composites via addition of magnetic crystals. *CrystEngComm* **2014**, *16*, 2097−2112.
(11) Xu, P.; Han, X. J.; Wang, C.; Zhao, H. T.; Wang, J. Y.; Wang, X. H.; Zhang, B. Synthesis of electromagnetic functionalized barium ferrite nanoparticles embedded in polypyrrole. *J. Phys. Chem. B* **2008**, *112*, 2775−2781.
(12) Lu, L. Y.; Xu, X. G.; Zhang, W. T.; Miao, J.; Jiang, Y. Enhanced magnetic properties of cobalt nanoparticles on FeMn films. *Mater. Lett.* **2010**, *64*, 2424−2426.
(13) Janaky, C.; Endrodi, B.; Hajdu, A.; Visy, C. Synthesis and characterization of polypyrrole−magnetite−vitamin B12 hybrid composite electrodes. *J. Solid State Electrochem.* **2010**, *14*, 339−346.
(14) Li, Q. L.; Zhang, C. R.; Wang, Y. X.; Li, B. D. Electromagnetic composite films based on polypyrrole hydro-sponge and Fe_3O_4 ferrofluid. *Synth. Met.* **2009**, *159*, 2029−2033.
(15) Watanabe, N.; Morais, J.; Accione, S. B. B.; Morrone, A.; Schmidt, J. E.; Martins Alves, M. C. Electronic, structural, and magnetic properties of cobalt aggregates embedded in polypyrrole. *J. Phys. Chem. B* **2004**, *108*, 4013−4017.
(16) Liu, Y. C.; Hwang, B. J. Enhancement of conductivity stability of polypyrrole films modified by valence copper and polyethylene oxide in an oxygen atmosphere. *Thin Solid Films* **2000**, *360*, 1−9.
(17) Liu, Y. C.; Tsai, C. J. Characterization and enhancement in conductivity and conductivity stability of electropolymerized polypyrrole/Al_2O_3 nanocomposites. *J. Electroanal. Chem.* **2002**, *537*, 165−171.
(18) Yavuz, Ö.; Ram, M. K.; Aldissi, M.; Poddar, P.; Hariharan, S. Synthesis and the physical properties of MnZn ferrite and NiMnZn ferrite−polyaniline nanocomposite particles. *J. Mater. Chem.* **2005**, *15*, 810−817.
(19) Yang, Y. C.; Pan, F.; Liu, Q.; Liu, M.; Zeng, F. Fully room-temperature-fabricated nonvolatile resistive memory for ultrafast and high-density memory application. *Nano Lett.* **2009**, *9*, 1636−1643.
(20) Gao, S.; Song, C.; Chen, C.; Zeng, F.; Pan, F. Dynamic processes of resistive switching in metallic filament-based organic memory devices. *J. Phys. Chem. C* **2012**, *116*, 17955−17959.
(21) Waser, R.; Dittmann, R.; Staikov, G.; Szot, K. Redox-based resistive switching memories nanoionic mechanisms, prospects, and challenges. *Adv. Mater.* **2009**, *21*, 2632−2663.
(22) Lampert, M. A. Simplified theory of space-charge-limited currents in an insulator with traps. *Phys. Rev.* **1956**, *103*, 1648−1656.
(23) Qiu, G. H.; Wang, Q.; Nie, M. Polypyrrole−Fe_3O_4 magnetic nanocomposite prepared by ultrasonic irradiation. *Macromol. Mater. Eng.* **2006**, *291*, 68−74.
(24) Liu, Y. C.; Tsai, C. J. Mechanism of conductivity decay of polypyrrole exposed to water and enhancement of conductivity stability of copper(I)-modified polypyrrole. *J. Electroanal. Chem.* **2002**, *537*, 165−171.
(25) Chen, A.; Wang, H.; Zhao, B.; Li, X. The preparation of polypyrrole−Fe_3O_4 nanocomposites by the use of common ion effect. *Synth. Met.* **2003**, *139*, 411−415.
(26) Liu, Y. C.; Hwang, B. J. Interaction of copper(I)−polypyrrole complexes prepared by depositing−dissolving copper onto and from polypyrroles. *Thin Solid Films* **1999**, *333*, 233−239.
(27) Pan, F.; Gao, S.; Chen, C.; Song, C.; Zeng, F. Recent progress in resistive random access memories: Materials, switching mechanisms, and performance. *Mater. Sci. Eng., R* **2014**, *83*, 1−59.
(28) Long, S. B.; Cagli, C.; Ielmini, D.; Liu, M.; Suñé, J. Reset statistics of NiO-based resistive switching memories. *IEEE Electron Device Lett.* **2011**, *32*, 1570−1572.
(29) Long, S. B.; Cagli, C.; Ielmini, D.; Liu, M.; Suñé, J. Analysis and modeling of resistive switching statistics. *J. Appl. Phys.* **2012**, *111*, 074508.
(30) Xu, Z. D.; Yu, L. N.; Xu, X. G.; Miao, J.; Jiang, Y. Effect of oxide/oxide interface on polarity dependent resistive switching behavior in ZnO/ZrO_2 heterostructures. *Appl. Phys. Lett.* **2014**, *104*, 192903.
(31) Liu, Q.; Long, S. B.; Lv, H. B.; Wang, W.; Niu, J. B.; Huo, Z. L.; Chen, J. N.; Liu, M. Controllable growth of nanoscale conductive filaments in solid-electrolyte-based ReRAM by using a metal nanocrystal covered bottom electrode. *ACS Nano* **2010**, *4*, 6162−6168.
(32) Yoon, J. H.; Han, J. H.; Jung, J. S.; Jeon, W.; Kim, G. H.; Song, S. J.; Seok, J. Y.; Yoon, K. J.; Lee, M. H.; Hwang, C. S. Highly improved uniformity in the resistive switching parameters of TiO_2 thin films by inserting Ru nanodots. *Adv. Mater.* **2013**, *25*, 1987−1992.